AGU PUBLICATIONS

JGR

Journal of Geophysical Research: Space Physics

RESEARCH ARTICLE

10.1002/2016JA022750

Key Points:
- Solar wind structures matching IPS observation, in situ measurement, and MHD equations are obtained
- Solar wind density and temperature at 50 Rs are determined through MHD-IPS tomography
- Density and temperature are expressed with parameterized functions of IPS-based solar wind speed

Correspondence to:
K. Hayashi,
keiji@sun.stanford.edu

Citation:
Hayashi, K., M. Tokumaru, and K. Fujiki (2016), MHD-IPS analysis of relationship among solar wind density, temperature, and flow speed, *J. Geophys. Res. Space Physics*, *121*, 7367–7384, doi:10.1002/2016JA022750.

Received 28 MAR 2016
Accepted 21 JUL 2016
Accepted article online 25 JUL 2016
Published online 3 AUG 2016

MHD-IPS analysis of relationship among solar wind density, temperature, and flow speed

Keiji Hayashi[1], Munetoshi Tokumaru[1], and Ken'ichi Fujiki[1]

[1] Institute for Space-Earth Environmental Research, Nagoya University, Nagoya, Japan

Abstract The solar wind properties near the Sun are a decisive factor of properties in the rest of heliosphere. As such, determining realistic plasma density and temperature near the Sun is very important in models for solar wind, specifically magnetohydrodynamics (MHD) models. We had developed a tomographic analysis to reconstruct three-dimensional solar wind structures that satisfy line-of-sight-integrated solar wind speed derived from the interplanetary scintillation (IPS) observation data and nonlinear MHD equations simultaneously. In this study, we report a new type of our IPS-MHD tomography that seeks three-dimensional MHD solution of solar wind, matching additionally near-Earth and/or Ulysses in situ measurement data for each Carrington rotation period. In this new method, parameterized relation functions of plasma density and temperature at 50 R_s are optimized through an iterative forward model minimizing discrepancy with the in situ measurements. Satisfying three constraints, the derived 50 R_s maps of plasma quantities provide realistic observation-based information on the state of solar wind near the Sun that cannot be well determined otherwise. The optimized plasma quantities exhibit long-term variations over the solar cycles 21 to 24. The differences in plasma quantities derived from the optimized and original IPS-MHD tomography exhibit correlations with the source-surface magnetic field strength, which can in future give new quantitative constrains and requirements to models of coronal heating and acceleration.

1. Introduction

The solar wind is a consequence of coronal heating and acceleration processes. Because dynamics of heating and acceleration have not been fully solved or well formulated, we need to introduce assumptions, such as uniform mass flux and constant gas pressure, to determine plasma quantities of the interplanetary plasma flow at a certain heliocentric distance well away from the solar corona and start models for solar wind. For example, many magnetohydrodynamics (MHD) models for super-Alfvenic solar wind [e.g., *Hayashi et al.*, 2006] need to specify the plasma density and temperature (or gas pressure) to start time-dependent MHD simulations; among the remaining variables, the magnetic field can be realistically extrapolated through the potential-field source-surface (PFSS) model [*Schatten et al.*, 1969; *Altschuler and Newkierk*, 1969] with observational data of solar photospheric magnetic field, and the plasma flow velocity can be determined through reliable models such as the Wang-Sheeley-Arge (WSA) model [*Arge et al.*, 2003].

The solar wind speed can be also determined from observations of interplanetary scintillation (IPS). The IPS is caused by electron density fluctuations in the solar wind. For a given IPS observation, we can determine a line-of-sight (LOS)-integrated value of solar wind speed through a correlation analysis of the scintillation signal detected at ground-based IPS facilities of Nagoya University. Several types of computer-assisted tomographic method [e.g., *Jackson et al.*, 1998; *Kojima et al.*, 1998; *Tokumaru et al.*, 2009; *Jackson et al.*, 2011] have been developed to reconstruct three-dimensional structures of solar wind from the IPS observation data.

One of them is the MHD-IPS tomography [*Hayashi et al.*, 2003]. In brief, this tomography is an iterative forward fitting method to seek the three-dimensional solution of eight MHD variables (density, temperature, three-component vectors of plasma flow, and magnetic field) that simultaneously satisfy the MHD equations and the IPS LOS observation data. Starting with a uniform solar wind distribution at a certain super-Alfvenic distance (set at 50 solar radii), a radial-marching MHD simulation is conducted to calculate the three-dimensional steady global solar wind structures. The IPS observations made in a Carrington Rotation (CR) period of interest are then simulated in this synthetic three-dimensional numerical solar wind data. In the last

process of one iteration step, the boundary solar wind distribution map is modified in a way such that the discrepancy between simulated and actual IPS observation will be decreased.

The radial-marching MHD simulation part in the IPS-MHD tomography also needs the boundary values of solar wind density and temperature on the inner boundary sphere to start the calculation. We used the empirical functions of solar wind speed, $N(V)$, and $T(V)$, derived from in situ measurement data at $r < 0.5$ AU by the Helios space probes in 1970s. Information on solar wind speed is provided from the IPS observations, and information on magnetic field is provided from solar surface magnetic field observations through the PFSS model; with the Helios-based empirical functions, all MHD variables in the MHD-IPS tomography are observation based. Overall, the relationship functions worked well for numerically making solar wind plasma quantities that are consistent with in situ measurements.

There are several reports, however, that the solar wind plasma measured in recent years are noticeably different from those modeled [e.g., *Riley et al.*, 2010]. From in situ measurements, *McComas et al.* [2008, 2013] reported that the solar wind plasma density measured by the Ulysses space probe in the solar minimum between solar cycles 23 and 24 are lower than that in the earlier minimum between the cycles 22 and 23. In the case of our IPS-MHD tomography, the Helios-based functions often yielded higher density and/or lower temperatures than near-Earth in situ measurements for periods after around 2007 [*Hayashi et al.*, 2011]. This difference implies that there arose differences in relationships, between solar wind speed and density and between speed and temperatures, and/or heating and acceleration processes in the solar corona, from those in the period of the Helios missions (solar cycle 21). Weaker solar polar photospheric magnetic field and resultant larger tilt angle of the heliospheric current sheet (HCS) [e.g., *Hoeksema*, 1995] in recent years is a candidate of the causes of the differences in solar wind plasma quantities. The north-south asymmetry found in global structures of solar wind speed from the IPS observations [e.g., *Tokumaru et al.*, 2010, 2015] is another manifest of the differences in solar coronal dynamics.

For addressing the dynamics behind the variations of solar wind plasma quantities found in the solar wind plasma, it is an important step to reconstruct the global structures of the solar wind as close to reality as possible. From a practical point of view in our IPS-MHD tomography, it is beneficial if we have other set(s) of relationship functions yielding plasma density and temperature better matching in situ measurements. Therefore, it is worth seeking optimal relationship functions, $N(V)$ and $T(V)$, that yield best agreements with the in situ data and hence the actual solar wind. An immediate approach is to parameterize the relationship functions and seek a set of optimal parameters for each solar rotation period and express them as functions of time, or other relevant parameters, such as magnetic field strength or proxy of coronal magnetic field structure, in addition to flow speed. Furthermore, such improved relation functions can represent the state of solar wind plasma near the Sun that cannot be well measured with remote sensing technique or space probes today; therefore, the modified functions can offer a good constraint or requirement to models of coronal heating and accelerations [e.g., *Usmanov et al.*, 2000, 2011; *Yang et al.*, 2016] and enhance MHD simulation models for the trans-Alfvenic solar corona [e.g., *Hayashi*, 2005; *Feng et al.*, 2010; *Riley et al.*, 2011; *Yang et al.*, 2012; *Feng et al.*, 2012, 2015; *Wu et al.*, 2016] and interplanetary space [e.g., *Dryer*, 1994; *Wu et al.*, 2005; *Kataoka et al.*, 2009; *Odstrcil and Pizzo*, 2009; *Intriligator et al.*, 2010; *Detman et al.*, 2011; *Wu et al.*, 2011; *Hayashi*, 2012; *Kim et al.*, 2014] and heliospheric models [e.g., *Washimi et al.*, 2011; *Pogorelov et al.*, 2013].

In this context, we recently developed an iterative optimization method to seek the optimal relationship functions, $N(V)$ and $T(V)$, that will yield better agreements with near-Earth in situ measurement data, Ulysses measurement data, or both near-Earth and Ulysses measurement data simultaneously, for each CR period. The steady state three-dimensional MHD solutions obtained will be probably best in a sense that the solution matches the in situ solar wind measurement in addition to the two constraints, MHD equations and IPS LOS solar wind speed observations, that are taken into account in the earlier version of MHD-IPS tomography. In this study, we apply this optimization to processing available measurement data over periods from CR 1645 (1976 August) until CR 2129 (2012 October) to test the ability of this optimization approach and to examine the variations of relationship among the plasma variables over three and half solar cycle periods.

2. Method and Data

2.1. MHD-IPS Tomography

In the MHD-IPS tomography [*Hayashi et al.*, 2003], the radial-marching MHD simulation is conducted for calculating the steady state of super-Alfvenic solar wind from 50 to 1250 R_s ($\simeq$5.8 AU) in the frame corotating

with the Sun. We use the Lax-Friedrichs-type strategy for calculating spatial derivatives in the latitudinal and longitudinal directions to advance in the radial direction to calculate a three-dimensional steady solution. The radial increment is done with two-step Runge-Kutta method. To start a radial-marching simulation we have to give a set of boundary values of all eight MHD variables at 50 R_s. The three components of magnetic field ($\vec{B}$) and plasma bulk velocity ($\vec{V}$) in the rotating frame are determined from the PFSS model, IPS data, and the zero-induction condition ($\vec{V} \times \vec{B} = \vec{0}$).

In order to determine density and temperature (or gas pressure), we determined the relationship function between temperature and flow speed, $T(V)$, at 50 solar radii as

$$T(V) = f_1 + f_2 \cdot \frac{V}{100}, \tag{1}$$

where $f_1 = -0.455$ and $f_2 = 0.1943$, and the relationship function between density and flow speed, $N(V)$, as

$$N(V) = f_3 + f_4 \cdot \left(\frac{V - f_5}{100} \right)^{f_6} \tag{2}$$

with

$$f_3 = 62.98, \quad f_4 = 866.4, \quad f_5 = 154.9, \quad \text{and} \quad f_6 = -3.402. \tag{3}$$

Here the solar wind speed V, number density N, and temperature T are given in units of km/s, count cm^{-3} , and 10^6°K, respectively. The expression of two equations ($T(V)$ and $N(V)$) and the six parameters ($f_1, \ldots, f_6$) are determined from the scatterplot of the in situ measurement data by Helios I and II at $r < 0.5$ AU [see *Hayashi et al.*, 2003, Figure 1] through the bi–least squares fitting.

The two parameters, f_1 and f_3, are the base values at zero speed. Because the solar wind is not of zero speed, the values at some lowest solar wind speed, for example, 250 km/s, represent the minimum values we here assume. The combination of f_3 and f_5 defines the position offset of the power law relation in the V-N space. The power law index, f_6, is always negative and determines the degree of nonlinear dependency of density on the solar wind speed: The smaller power index means the relative plasma density is higher at slow solar wind regime, and the larger index means the density is less dependent on speed.

Starting from a uniform distribution as an initial guess, the boundary plasma variables at 50 R_s are modified in a way such that the differences between the actual IPS observational data and synthetic LOS-integrated flow speed calculated in the three-dimensional steady solar wind solution will be reduced. This process, consisting of conducting MHD simulation, making synthetic IPS measurement, and modifying the 50 R_s boundary plasma quantities, is repeated until the total residuals between synthetic LOS integrations and actual IPS velocity data converged. The radial component of magnetic field (B_r) at 50 R_s is fixed all through the process of the MHD-IPS tomography. Here we note that the tomographic method seeks the solutions of undisturbed, steady state of the solar wind. To obtain the steady state better, the IPS data of interplanetary disturbances must be excluded. To exclude objectively the data of disturbance, the MHD-IPS tomography first conducts provisional iterations and then discards the IPS LOS data when the difference between synthetic and actual LOS velocities is significantly large. Using the selected IPS data set, the MHD-IPS tomography finally yields the three-dimensional MHD solutions of quiet solar wind. Usually, a satisfactorily converged solution is obtained after 15 iterations. Figure 1 shows the distributions of steady state solar wind density and speed at 50 and 215 R_s obtained for a period of CR 2008 as an example.

This original version of our MHD-IPS tomography [*Hayashi et al.*, 2003] uses the data of IPS observation and the synoptic maps of the solar photospheric magnetic field from Wilcox Solar Observatory (WSO) (http://wso.stanford.edu) [e.g., *Hoeksema et al.*, 1983]. Near-Earth or Ulysses in situ measurement data were used for validation, but not in processes of the MHD-IPS tomography. In the next section, we use in situ measurement data of solar wind plasma as an additional constraint in seeking an MHD solution of steady state solar wind.

2.2. Optimization of Relationship Functions

First, for simplicity, we assume that the form of functions, $N(V)$ and $T(V)$, will not be altered from those we defined in the original version of the MHD-IPS tomography. Instead, the six parameters of equations (1) and (2) will be modified, in a way such that better agreements with in situ measurement will be obtained.

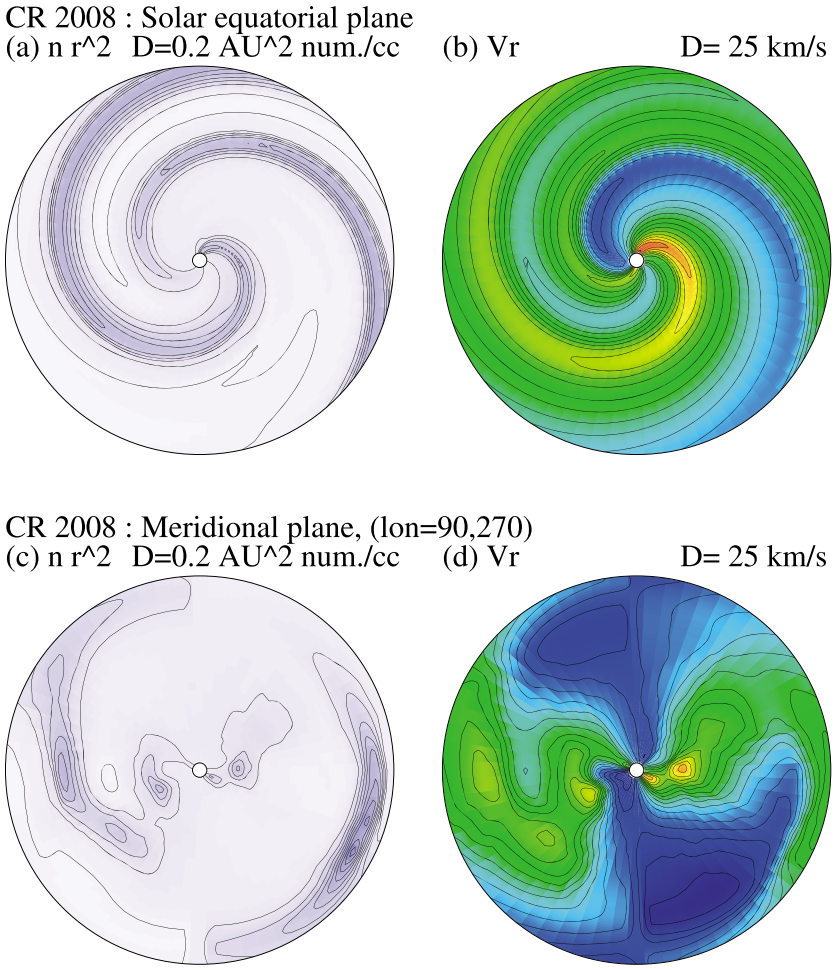

Figure 1. Solar wind density and radial component of plasma flow, on the (a, b) equatorial plane and a selected (c, d) meridional plane. In Figures 1b and 1d, blue, yellow, and orange colors approximately represent plasma speed of 700, 500, and 300 km/s, respectively. The contour curves are placed with fixed interval of 0.2 $(AU)^2$ count/cm^3 for number density normalized with r^2, and 25 km/s for speed.

In this study, we choose the mean square error (MSE) as a proxy of the total discrepancy [e.g., *Owens et al.*, 2005] between a simulated three-dimensional steady state solar wind and a set of target in situ measurement data. Denoting the MSE as D, the discrepancies in temperature and density are given as

$$D_T(f_1,\ldots,f_p) = \frac{\sum_i^m (T_{\mathrm{sim}}(f_1,\ldots,f_p;r_i,\theta_i\,\phi_i) - T_{\mathrm{in\ situ}}(i))^2}{\sum_i^m T_{\mathrm{in\ situ}}^2(i)} \tag{4}$$

$$D_N(f_1,\ldots,f_p) = \frac{\sum_i^m (N_{\mathrm{sim}}(f_1,\ldots,f_p;r_i,\theta_i\,\phi_i) - N_{\mathrm{in\ situ}}(i))^2}{\sum_i^m N_{\mathrm{in\ situ}}^2(i)}, \tag{5}$$

respectively, where p is the number of free parameters ($p=6$ in this study) and m is number of in situ measurements available for a period under optimizing calculation. We use daily averaged in situ measurement data, and the time span for a MSE calculation is set to be 1 CR period.

In this study, we conduct three types of optimizations; seeking a best agreement with the near-Earth data set (hereafter, labeled as Choice E), with the Ulysses data (Choice U), or both (Choice B). The number of in situ data, m, is up to 27 or 28 for Choices E and U, and 54 to 56 for Choice B, if there are no data gaps. When comparing with the Ulysses data, the time window is shifted a half CR period backward to take into account an approximate travel time from 50 R_s to 1.3–6 AU. Additionally, to adjust decreases of density and temperature with heliocentric distance in the Ulysses data, we normalize density and temperature as $N \times r^2$ and $T \times r$, respectively. These normalizations implicitly assume that the solar wind plasma is polytropic, and the specific

heat ratio (γ) is close to 1.5. We used the number derived from Helios data analysis [*Totten et al.*, 1995] and set $\gamma = 1.46$. The computation time of one MHD-IPS tomography run is typically one or a few minutes on an ordinary computer, depending on the number of IPS LOS data in the CR period of interest and the fastest (largest) eigen velocity of the hyperbolic MHD equation system in the latitudinal and longitudinal directions.

The optimization employs an iterative strategy and concepts of the gradient descent method and the Newton-type method. Let n be the step number of iteration of optimization, with the initial guess represented as $n=0$. The initial guess parameters, $f_1^0, \ldots, f_6^0$ are set equal to those of the Helios-based relation functions (equation (3)). At each step, an increment of the ith parameter from the nth iteration step, $(f_i^{n+1} - f_i^n)$, is calculated from the ratio of the first-order derivative and the absolute value of the second-order derivative,

$$\left(\frac{\partial D}{\partial f_i}\right)^n \sim \frac{D(f_1^n, \ldots, f_i^n + \Delta f_i^n, \ldots, f_6) - D(f_1^n, \ldots, f_i^n - \Delta f_i^n, \ldots, f_6)}{2 \cdot \Delta f_i} \tag{6}$$

and

$$\left|\frac{\partial^2 D}{\partial f_i^2}\right|^n \sim \frac{D(f_1^n, \ldots, f_i^n + \Delta f_i^n, \ldots, f_6^n) - 2D(f_1^n, \ldots, f_6^n) + D(f_1^n, \ldots, f_i^n - \Delta f_i^n, \ldots, f_6^n)}{(\Delta f_i)^2}. \tag{7}$$

To obtain all discrepancy values needed, we need in total 13 MHD-IPS tomography runs. One of 13 is done with a set of central values $(f_1^n, \ldots, f_6^n)$ already calculated at the previous step n. The remaining 12 runs are for differencing in the discretized parameter space, that is, $(f_1^n + \pm\Delta f_1, f_2^n, \ldots, f_6^n)$, …, $(f_1^n, f_2^n, \ldots, f_6^n \pm \Delta f_6)$. The two parameters for temperature, f_1 and f_2, are updated as

$$f_i^{n+1} = f_i^n - (\Delta f_i) \cdot \frac{0.4}{\sqrt{2}} \frac{(\partial D_T/\partial f_i)^n}{|\partial^2 D_T/\partial f_i^2|^n}, \tag{8}$$

and the rest four parameters for density, $f_3, \ldots, f_6$ are updated as

$$f_i^{n+1} = f_i^n - (\Delta f_i) \cdot \frac{0.4}{\sqrt{4}} \frac{(\partial D_N/\partial f_i)^n}{|\partial^2 D_N/\partial f_i^2|^n}. \tag{9}$$

By taking the absolute value of second-order derivative at denominator, the iteration will seek only the minima nearby the initial guess, without being attracted toward maxima. We add a small number (10^{-3}) to the denominator to avoid zero value at inflection or saddle point that seldom arises. The factor 0.4 is set for sake of computational stability.

It should be noted that there is a cross-talk effect among the simulated MHD variables in the MHD-IPS tomography part and the function parameters under optimization. For example, the modification of first two parameters (for $T(V)$) alters the simulated speed of polytropic solar wind at distant regions; hence, the MHD-IPS tomography yields different velocity map at 50 R_s. Similarly, the modification of the rest four parameters (for $N(V)$) alters the values of simulated IPS LOS-integrated speed then the boundary velocity values. The inner-boundary B_r is fixed all through the optimization and the MHD-IPS tomography, but the values of B_r at the positions of in situ measurement can be altered as the result of changes in the plasma speed. This cross-talk effect is a natural character of this optimization process for the nonlinear MHD system, and we confirmed that these cross-talk effects, with the factor 0.4 at equation (9), do not cause any computational instabilities in a course of the optimization process.

2.3. Data and Examined Period

To calculate the residuals, D_T and D_N, between a steady MHD solution and in situ measurements, we use the two data sets, the OMNI data set for the near-Earth measurement and the COHO data set for the in situ measurement data by the Ulysses space probe. To start the MHD-IPS tomography, we use the magnetogram synoptic map data and IPS data. From around middle 1970s, we have sufficient number of the IPS observation data, and the solar photospheric magnetic field data (in this study, the WSO) with minor data gaps. The near-Earth in situ measurement data compiled and organized at the OMNI database at Goddard Space Flight Center (GSFC)/NASA provides good temporal coverage. The Ulysses data at COHO database at GSFC/NASA covers the mission time span, from late 1991 to middle 2008.

Table 1. Numbers of Carrington Rotation Periods Examined

CR Numbers	Near Earth (Choice E)	At Ulysses (Choice U)	Both (Choice B)
1654–1699	11 (1)	—	—
1700–1749	11	—	—
1750–1799	18	—	—
1800–1849	37	11 (1)	11 (1)
1850–1899	22 (1)	22 (1)	22
1900–1949	31 (1)	31	31
1950–1999	32 (1)	32	32
2000–2049	28 (1)	28	28
2050–2100	17 (1)	17	17
2100–2129	8	—	—
Total	216 (6)	141 (2)	141 (1)

Out of 487 CR periods from CR 1645 (1976 August) to CR 2131 (2012 December), we had 216 CR numbers that satisfy two criteria we set for sake of computational stability: (1) 150 or more line-of-sight IPS data were made over a CR period and (2) 10 or more daily averaged in situ data values are available in the OMNI data set. As for the Ulysses mission data, from CR 1835 to CR 2086, we have 141 satisfying CR periods.

For all examined CR periods, Choice H (the MHD-IPS tomography using the Helios-based functions without optimization) gave steady state solutions of the solar wind. The optimization with Choice E yielded converged solutions for 210 CR periods out of the selected 216 periods. The failed six periods are CR1694, 1871, 1902, 1957, 2036, and 2072. The optimizations to the Ulysses data (Choice U) yielded converged solutions for 139 CR periods out of 141. The two failures are for CR 1835 and 1856. The optimizations for both Ulysses and near-Earth in situ measurements (Choice B) gave solutions for 140 CR periods with one failure for CR1835. All failures, nine in total, are due to a convergence to an obviously unrealistic attractor around a local minimum where the MSE is much larger than the initial guess (Choice H). In these failed periods, IPS observations often do not cover regions near the high-latitude region in the southern hemisphere.

Table 1 summarizes the numbers of examined, successful and failed optimizations, every 50 CR periods (approximately 4 years). The CR periods of successful (failed) cases are indicated with filled (open) circles in Figures 5 and 6.

3. Results

3.1. Optimization

Figure 2 compares the 50 R_s maps of number density, temperature, flow speed, and radial component of magnetic field obtained with Helios-based parameters (Choice H) and optimized ones for the near-Earth in situ measurement data (Choice E), for CR 2008 as an example. In this example, the density contrast was overall enhanced: The slow-wind belt near the heliospheric current sheet (HCS) at low-latitude regions increases in density and size, while the density in high-latitude fast-wind regions decreased. On the other hand, the temperature overall increased. We can also see minor difference in the flow speed at 50 R_s that is due to the changes in density and temperature.

Figure 3 compares the solar wind quantities at the Earth and the Ulysses space probe in two selected periods, CR 1982 and 2076. In each plot, thick green, blue, and red lines show the values of in situ data, values derived from Choice H, and Choice E or Choice U. From Figure 3, we see that the differences from in situ data are indeed reduced through the optimization process. The solar wind speed at the positions of in situ measurement did not noticeably change, which is expected because the IPS LOS observations for r <1 AU well constrain the plasma speed in three-dimensional MHD solutions at 1 AU and beyond.

It is important to check the influence of uncertainty in the input data on the results. The uncertainty in IPS LOS velocity is estimated from uncertainty of time lag of scintillation power amplitude among three IPS observation facilities, and the averaged uncertainty is about 10% of the derived most plausible value. Using this uncertainty number of IPS LOS data, we conducted test analyses using synthetic IPS data sets prepared by

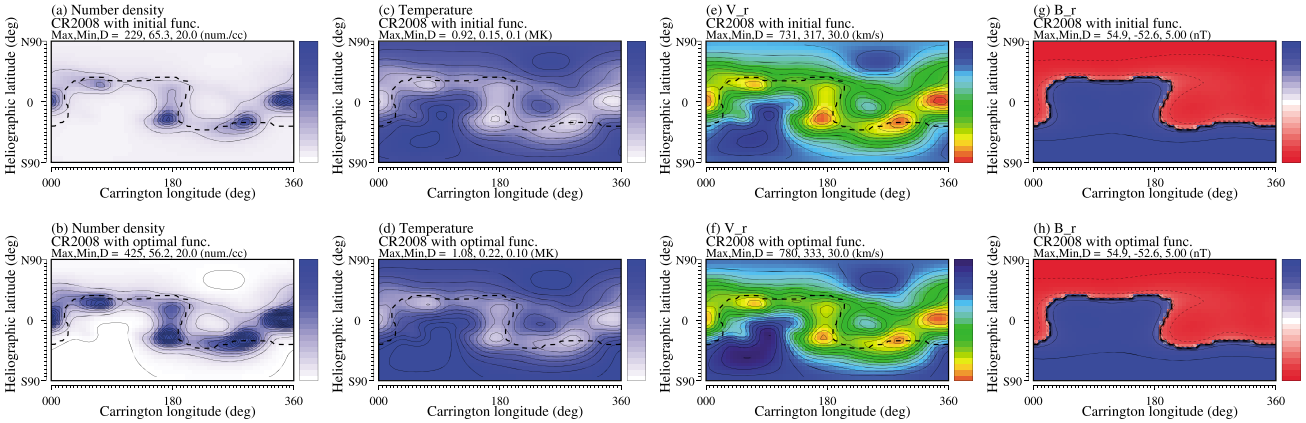

Figure 2. Solar wind density, temperature, the radial component of plasma flow, and magnetic field on the inner boundary sphere at 50 R_s. (a, c, e, and g) Obtained from our ordinary MHD-IPS tomography (Choice H) and used as an initial guess values for the optimization. (b, d, f, and h) Optimized maps from Choice E. Notice that the magnetic field maps (Figures 2g and 2h) are identical to each other. The flow speed, which is not subject to the optimization, changes slightly. In this example (CR 2008), density at slow-speed region near the HCS increases, while density at high-speed regions away from the HSC decreases. The temperature increases all over the map in this case. In Figures 2e and 2f, blue, yellow, and orange approximately represent plasma speed of 700, 500, and 300 km/s, respectively.

randomly increasing or decreasing each LOS velocity value with average absolute modulation of 10% of the original value. The 10 thin lines in each box of Figure 3 show the numerical solutions derived through the identical codes of IPS-MHD tomography and its optimization algorithm but using the randomly modulated IPS LOS velocity data set, for CR 1982 and 2076. The derived solar wind solutions with randomized inputs scatter around the thick curves (with nonrandomized, original IPS LOS data). A noticeable point is that blue lines (from original IPS analysis) and red lines (from optimization shown in this study) for density and temperature are distinguishably different; hence, we can claim here that the optimization can improve the relationship functions $N(V)$ and $T(V)$ in a way less sensitive to the uncertainty in input data. As for the flow speed, the red and blue lines run within limited ranges (roughly $\pm$50 km/s) around the values derived from nonrandomized original IPS data. This is a natural consequence of tomographic method: The randomized modulations are moderately canceled out in each MHD-IPS tomography process. The scatter widths of the variables are about 10% (mostly equal to the randomization amplitude for LOS velocity data), for both solo IPS-MHD tomography (red lines) and the optimization process. As seen in Figure 3l, the temperature at the position of Ulysses is much scattered, probably because the flow-flow interactions enhanced the scatters in a course to the heliocentric distance of about 4 AU.

3.2. Changes in MSE and Correlation Coefficients

Figure 4 shows the MSE and correlation coefficients of variables (N, T, V_r, and B_r), mapped with the values from Choice H in abscissa and those from the optimized functions in ordinate. It is clearly noticed that the MSE of the density and temperature were reduced for almost all CR periods in Choices E and U through the optimization process as it is designed. The values of MSE of solar wind speed (Figures 4c and 4g) exhibit even scatters across the diagonal line, which means that overall no significant improvement or deterioration.

The wider range of scatter of points in Figure 4g (Choice U) than in Figure 4c (Choice E) is primarily due to the cases where the optimization tries to reach better agreements with high temperatures at the Ulysses positions during its first and third high-latitude passages. The obtained higher temperatures at 50 R_s result in higher temperatures at $r > 1$ AU, while the MHD-IPS tomography itself does not use the solar wind speed at $r > 1$ AU to modify the boundary values of speed. This is a point we would improve in the future: The decrease of solar wind temperature with respect to the heliocentric distance might be different from that described with the polytrope assumption with specific heat ratio ($\gamma = 1.46$), at least at high-latitude regions and at the minimum phase of solar activity. In particular, substantial amount of heating flux supplied from the Sun may reach distant regions along less curved magnetic field lines near the solar rotational axis.

The MSE values of the radial component of magnetic field (B_r) in Figures 4d and 4h did not change significantly, primarily because 50 R_s maps of B_r are not modified in a course of optimization.

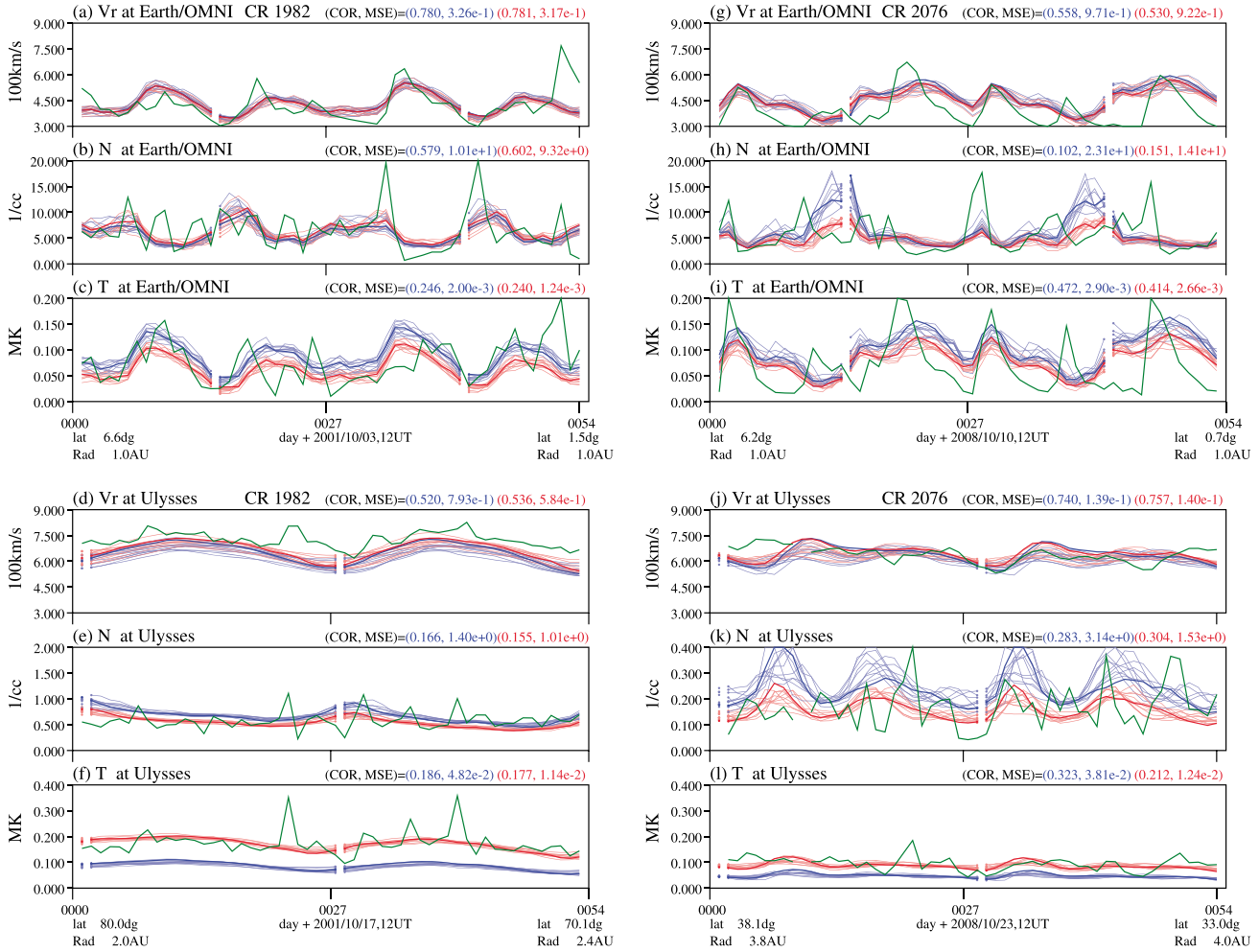

Figure 3. Examples of comparison of the calculated solar wind with in situ measurements. (a–c) Comparison of the flow speed, density, and temperature derived from Choice E with those of near-Earth OMNI data set, for a period of CR 1982. (d–f) Comparison of the three variables derived from Choice U with those of Ulysses in situ data. (g–l) The same comparisons as Figures 3a–3f but for another selected period, CR 2076, are shown. In each box, thick green, blue, and red curves show the in situ measurement data, the simulated variables from Choice H at the positions of each in situ measurement, and the optimized variables from Choice E or U, respectively. Notice that the red lines (with optimized functions) are much closer to the green lines (in situ data) than the blue lines (Choice H) are. Thin lines colored with brighter red or blue are for results from Monte Carlo-type tests, in each of which randomly modulated IPS velocity data are used.

In the correlation coefficients shown in Figures 4i–4p, we do not see significant improvement or worsening: The scatters are overall along the diagonal line. This is not a surprise or disappointment: The optimization does not significantly alter the shape (or contour pattern) of distribution of solar wind speed map at 50 R_s, and the plasma density and temperature at 50 R_s are monotonic functions of flow speed; hence, the temporal profile of plasma quantities at the positions of in situ measurements do not vary significantly through the optimization (see in Figure 2). The phase of temporal profile can be altered mainly due to the changes of flow speed, which can result in both increase and decrease of correlation coefficients.

3.3. Changes in Temperature and Density

Figure 5 compares the simulated plasma temperature, density, and flow speed with in situ measurements. In Figure 5 (left column), the solar wind variables derived from Choice H (blue), Choice E (green), and near-Earth in situ data (green) averaged over one CR period are shown. In Figure 5 (right column), the same format is applied to compare Choice H, Choice U, and Ulysses in situ data. We can see overall improvement in agreements with in situ data, as the optimization procedure is designed.

Choice E yields the series of MHD solutions that better trace the near-Earth data than Choice H does, with an exception of a spike of density (marked with (A)). We have better agreeing density at the declining phase of solar cycle 22 (marked as (B)), for which we had obtained lower values from Choice H.

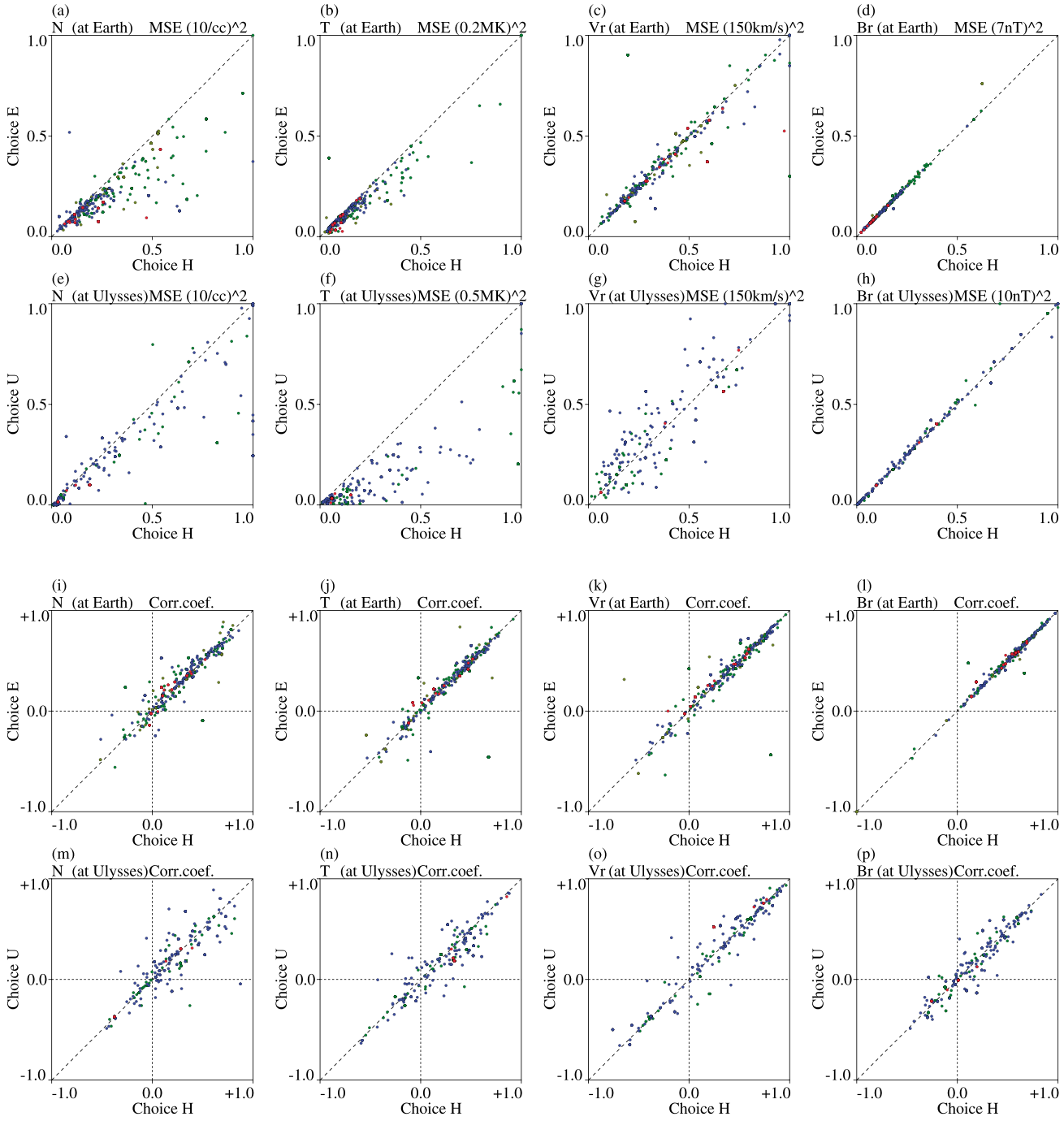

Figure 4. The values of MSE for (a) density, (b) temperature, (c) speed, and (d) the radial component of magnetic field obtained in Choice H and Choice E are placed in the scatterplot. (e–h) The MSE values from Choice H and Choice U are mapped in the same format as Figures 4a–4d. In the MSE plots, a mark below the diagonal dashed line corresponds to a case where the MSE was reduced through the optimization. (i–p) The correlation coefficients are mapped in the same format as Figures 4a–4h except that a mark above the diagonal dashed line means a case where the correlation was increased.

Functions optimized to the Ulysses measurement (Choice U) give good agreements in density, and significant improvements in temperature. Specifically, the density at the first and third high-latitude passages (marked as (C) and (D) in the plot), the low density at the fast wind at high-latitude regions, and the increases of density at the passage of solar equator are well reconstructed. Temperatures are also improved significantly; however, we notice that still the optimized temperature functions gave somewhat lower values than the actual in situ data in the first travel to high-latitude (southern) region (marked as (E)) in the solar cycle 22.

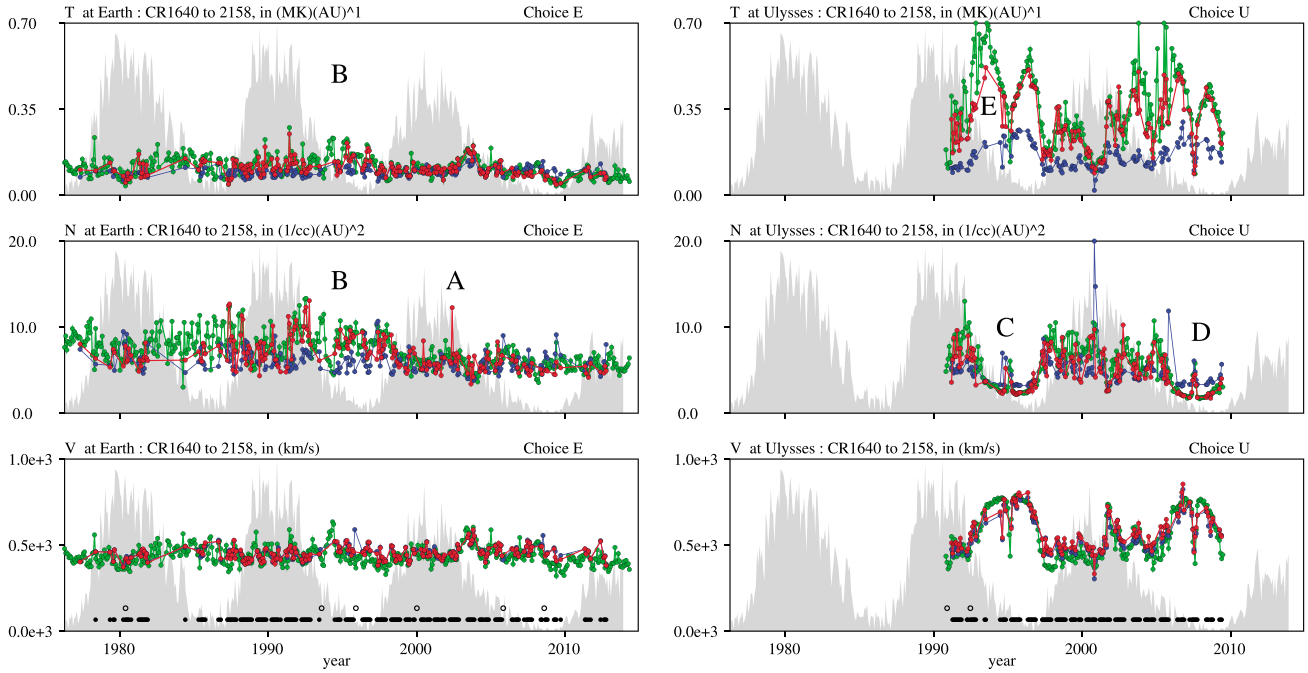

Figure 5. Temperature, number density, and plasma flow speed at the positions of in situ measurements averaged over one Carrington Rotation period. (left column) The averaged values of the in situ data (green), MHD variables from Choice H (blue), and from Choice E (red) at the position of Earth are drawn. (right column) The averages of Ulysses data, Choice H, and Choice U at the positions of Ulysses space probe are drawn. Each plot covers period of three and a half solar cycles, and the monthly sunspot numbers (from http://sidc.oma.be/silso/DATA/monthssn.dat) are drawn as the background gray for reference. In Figure 5 (bottom row), small filled (open) circles are placed at positions of CR numbers for which the optimization process succeeded (failed).

The averaged flow speeds V_r did not significantly differ, which proves that manipulating the density and temperature did not cause undesired side effects in determination of the solar wind speed that is primarily constrained by hundreds of LOS-integrated IPS data values.

Figure 6 shows the comparisons for Choice B in the same format as in Figure 5. Overall, the obtained averaged values tend to place between Choices E and U. Hence, Choice B is not the best one for determining the solar wind parameters either near the Earth or at the position of Ulysses; however, Choice B can give solutions that are constrained by more observation and measurement than the other two choices are, and it is a best foundation for achieving the most comprehensive descriptions of three-dimensional solar wind structures.

3.4. Variation of Shapes of Relationship Functions Over Solar Cycles

Figure 7 shows shapes of $N(V)$ and $T(V)$ at 50 R_s over the period of the Ulysses mission, for which we can perform all of the three types of optimization (Choices E, U, and B). In each pair of boxes, the optimized relationship functions $N(V)$ and $T(V)$ over a 40-CR period (approximately 3 year period) are drawn with red curves, superimposed with a blue curve that shows the Helios-based function. Overall, the red curves fall nearby the blue curve.

Among similarities in tendency found in the three choices, a most noticeable one is that at Figures 7f, 7l, and 7r (for a period from CR 2040 to 2079 or from 2006 February to 2009 January), the solar wind density at slow wind (~300 km/s) is lower than the reference Helios-based function. This is consistent with the analysis of IPS fluctuations by *Tokumaru et al.* [2012]. A noticeable temporal variation trend is found in Figures 7a–7f (Choice E) that the density and temperature at 50 R_s at the beginning (1990s) tend to be higher than those at the Helios era of 1970s, then exhibit gradual decrease with time, and finally become lower in 2000s. Figure 8 shows the six free parameters optimized with Choices E, U, and B as functions of time. We notice that the sixth parameter (f_6, a negative power index) decreases noticeably in the last part of the Ulysses mission period (marked with a cross), which results in steeper gradient and lower values of N at small values of V than in Choice H.

In the right plots of Figures 7a–7f, the temperature at 50 R_s from Choice E exhibits a long-term variation: It is hotter than the Helios-based line in early part of this plotted period and then gradually decreases to below the Helios-based line in the last 40-CR period. On the other hand, the temperature function from Choices U

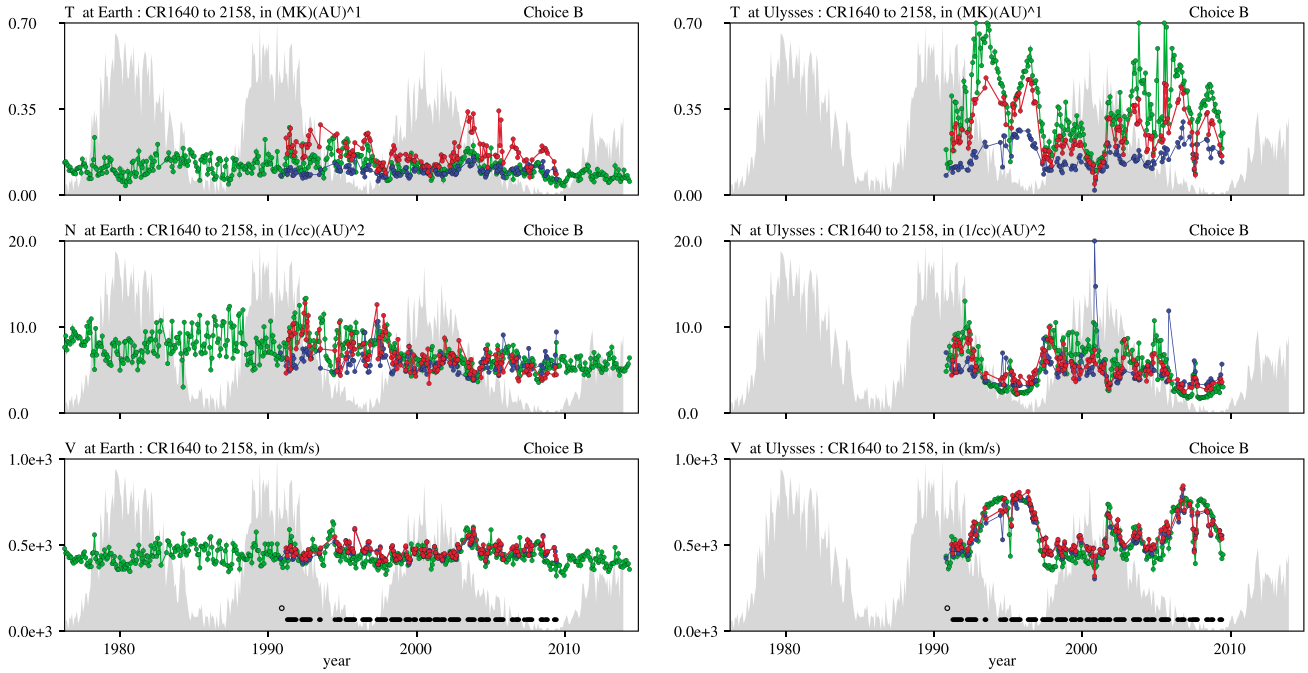

Figure 6. Same as in Figure 5 but the simulated values at positions of in situ measurements are from Choice B.

or E yields higher values than the Helios function for all periods plotted. Probably, there are some heating processes that remain at distant regions ($r \geq 50R_s$) and/or in high-latitude regions, and/or our MHD part assuming a constant specific heat ration ($\gamma = 1.46$) without any heating processes could not well reproduce the temperature at Ulysses positions.

4. Summary and Discussion

This paper describes the method to reconstruct numerically three-dimensional MHD solution of solar wind that best matches the three constraints, MHD equations, LOS IPS observation, and in situ measurement(s). The parameterized relation functions, $N(V)$ and $T(V)$, can determine the solar wind plasma quantities at 50 R_s that cannot be well determined otherwise.

The optimized functions differ for different target in situ measurements in different CR periods. Therefore, the derived relation functions do not immediately provide unified descriptions on dynamics of solar wind and solar corona in the global scale. Instead, we can use Choice E for studies of the Sun-Earth connection, such as those in the space weather paradigm. Choices U and B will give observation-based and theory-based constraints for assessing the dynamics of the solar wind heating and accelerations and the energy fluxes remaining at $r > 1$ AU that should be taken into account in the MHD and other solar wind models in the future. In particular, Choice B can be a basic framework for developing a unified description of solar wind dynamics in the global heliosphere, from the northern to southern pole and from the solar surface to heliopause.

In Figure 8, a tenth-order polynomial fitting curve is placed for each of six optimized parameters in each choice. Table 2 tabulates the coefficients of the polynomials in a form, $\sum_{i=0}^{10} a_i \tau^i$, as function of a normalize time τ that is defined as $\tau = (t - t_{CRs})/(t_{CRe} - t_{CRs})$ with the start date t_{CRs} set at 21:36 UT 16 April 1976 (the central time of CR 1640) and the end date t_{CRe} at 06:43 UT 22 December 2014 (the central time of CR2158). The coefficients from Helios in situ data (Choice H) are placed in the table for reference. With these, we can determine the plasma density and temperature as functions of flow speed and time, $N(V, t)$ and $T(V, t)$. These polynomial expressions can be used as a convenient form to determine the boundary values of plasma density and temperature in interplanetary models.

In Figure 8, the six parameters display various types of long-term variations over the solar cycles 21 to 24. In addition to the noticeable decrease in recent years, the power law index (f_6) is overall higher than the reference Choice H during the solar cycles 22 and 23. The increased values indicate that the plasma density was less

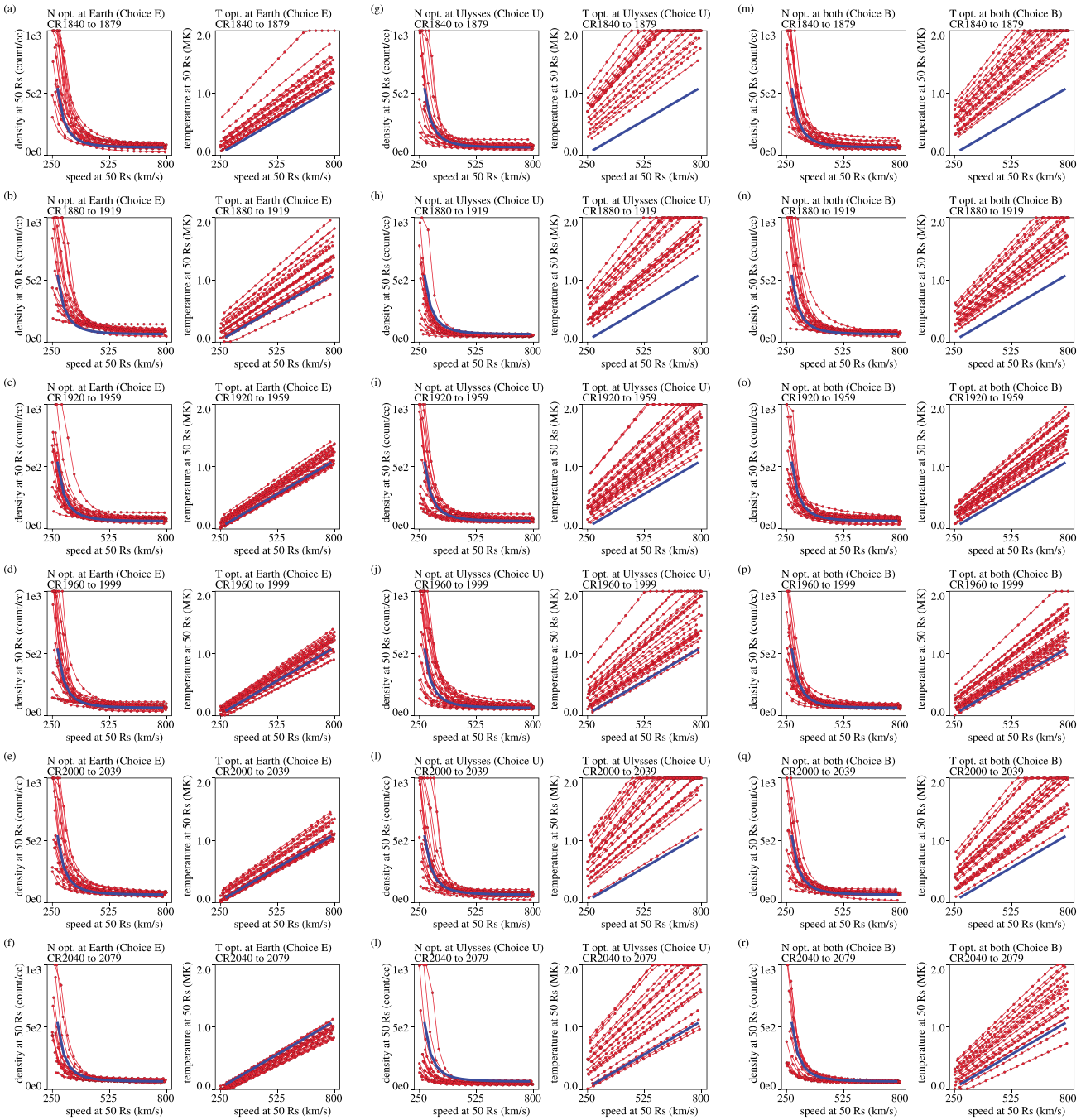

Figure 7. Relationship functions $N(V)$ and $T(V)$ obtained from Choices (a–f) E, (g–l) U, and (m–r) B, from CR 1840 to 2079. In each pair, the density (temperature) function is drawn in the left (right) box. Each box superimposes the optimized functions for all successful CR numbers with red line. A blue line showing the Helios-based function is drawn for reference.

sensitive to the solar wind speed, and the fast solar wind in the cycles 22 and 23 was of higher relative density than in recent years. In Choice U, the power law index appears to correlate with the sunspot numbers during the cycle 22 and 23, probably because two of three passages of the Ulysses in high heliographic latitudes took place during the solar minimum activity phase, for which the relatively uniform solar wind there resulted in somewhat large uncertainty in optimization process for Choice U. Nonetheless, the decrease of f_6 seen in the last solar minimum between the cycles 23 and 24 might be real because all three Choices show the same trend (marked with a cross in Figure 8). The two parameters for temperature (f_1 and f_2) were another set of parameters that exhibit long-term trend. These two parameters were, in all three choices, overall higher in the

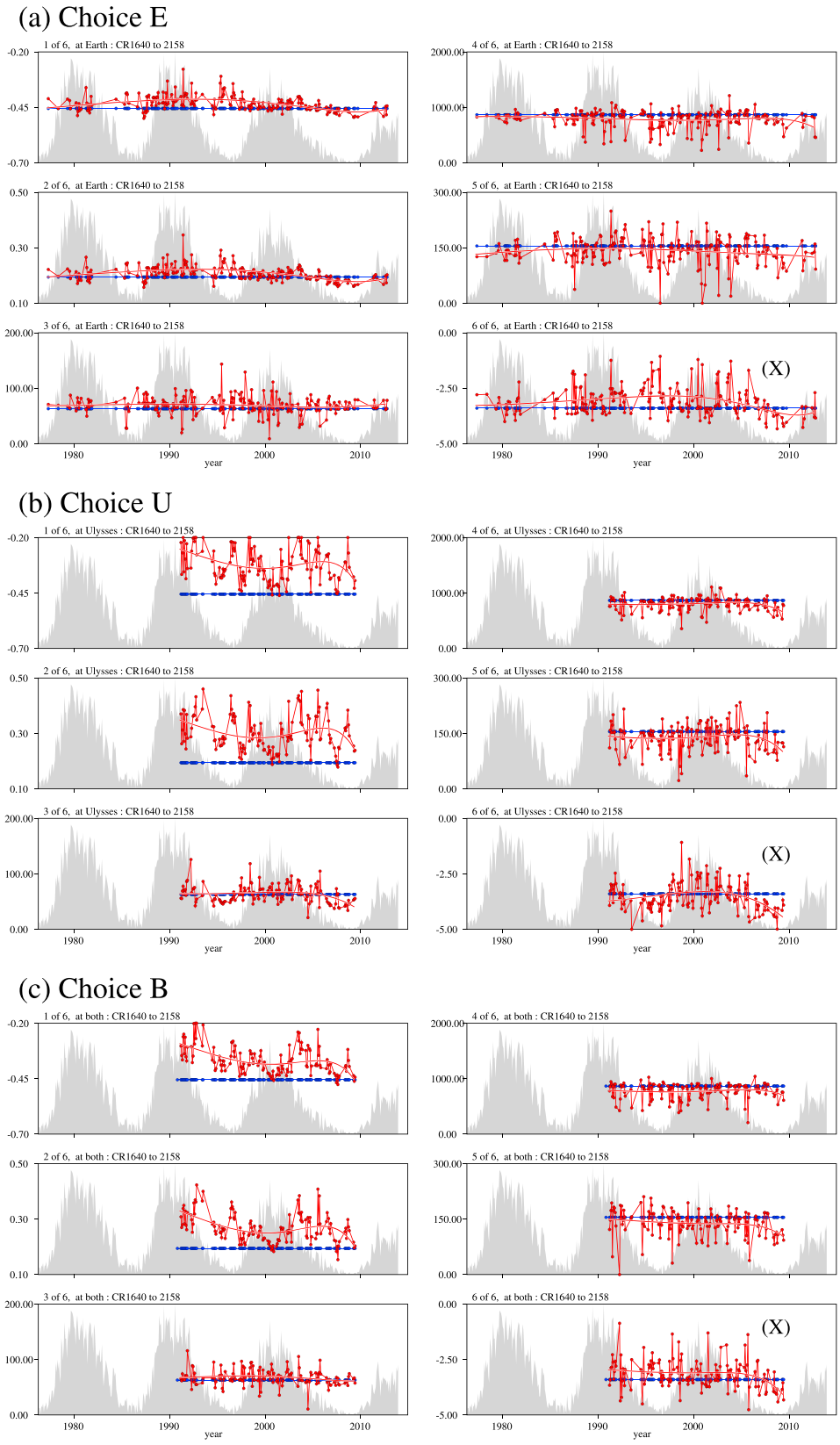

Figure 8. The six parameters optimized with Choices E, U, and B, as function of time. Blue horizontal lines are the set of initial parameters (Choice H). Red lines connecting circles are for the optimized parameters. A tenth-order polynomial fitting curve is placed in each box to show the long-term trends.

Table 2. Parameters as Functions of Normalized Time

	(H)	0	1	2	3	4	5	6	7	8	9	10
						Choice E						
$(f_1 + 0.7)/0.5$	(0.4890)	0.4880	0.2817	0.0034	−0.2931	−0.3464	−0.1899	0.0318	0.1953	0.2404	0.1614	−0.0157
$(f_2 - 0.1)/0.4$	(0.2358)	0.2308	0.2317	0.0351	−0.2306	−0.2998	−0.1978	−0.0421	0.0813	0.1463	0.1712	0.1946
$f_3/200.0$	(0.3149)	0.3391	0.0549	0.0615	−0.1167	−0.2518	−0.1736	0.0776	0.3368	0.4157	0.1605	−0.5274
$f_4/2000.0$	(0.4332)	0.4156	0.0429	−0.2331	−0.1274	0.1355	0.3170	0.3142	0.1462	−0.1008	−0.3224	−0.4265
$f_5/300.0$	(0.5163)	0.4348	0.2735	−0.1748	−0.3209	−0.1627	0.1036	0.2823	0.2770	0.1050	−0.1355	−0.3096
$(f_6 + 5.0)/5.0$	(0.3196)	0.3411	0.0979	0.1974	0.1261	−0.0439	−0.2984	−0.5694	−0.7090	−0.5206	0.2001	1.6330
						Choice U						
$(f_1 + 0.7)/0.5$	(0.4890)	1.1744	−0.2272	−1.1256	−0.9682	0.1168	1.5716	2.6983	2.8285	1.3980	−2.0305	−7.7673
$(f_2 - 0.1)/0.4$	(0.2358)	0.9214	−0.2984	−1.1063	−0.9416	0.1434	1.6477	2.8698	3.0766	1.5916	−2.1688	−8.6843
$f_3/200.0$	(0.3149)	0.3513	−0.0686	−0.1297	0.0917	0.3299	0.3595	0.1058	−0.3380	−0.7283	−0.6917	0.2647
$f_4/2000.0$	(0.4332)	0.4074	0.0376	−0.1555	−0.1090	0.0923	0.3108	0.4216	0.3395	0.0217	−0.5360	−1.3043
$f_5/300.0$	(0.5163)	0.5648	−0.1167	−0.3722	−0.1281	0.3606	0.7616	0.8298	0.4664	−0.2768	−1.2115	−2.0252
$(f_6 + 5.0)/5.0$	(0.3196)	0.2362	−0.0873	0.1020	0.4906	0.6188	0.2344	−0.5915	−1.4836	−1.8179	−0.7638	2.6981
						Choice B						
$(f_1 + 0.7)/0.5$	(0.4890)	1.0928	−0.2406	−1.0777	−0.9150	0.1015	1.4384	2.4531	2.5485	1.2351	−1.8555	−6.9766
$(f_2 - 0.1)/0.4$	(0.2358)	0.8966	−0.3267	−1.1523	−1.0106	0.0610	1.5780	2.8493	3.1370	1.7351	−2.0026	−8.6596
$f_3/200.0$	(0.3149)	0.2806	0.1312	0.0531	0.0179	−0.0300	−0.1198	−0.2350	−0.3133	−0.2527	0.0845	0.8713
$f_4/2000.0$	(0.4332)	0.4039	0.0584	−0.1795	−0.2007	−0.0203	0.2668	0.5290	0.6184	0.3748	−0.3781	−1.8417
$f_5/300.0$	(0.5163)	0.5105	0.1222	−0.2548	−0.3916	−0.1951	0.2656	0.7928	1.0978	0.8248	−0.4382	−3.1605
$(f_6 + 5.0)/5.0$	(0.3196)	0.4429	0.0414	−0.2718	−0.3091	−0.0406	0.4190	0.8587	1.0095	0.5679	−0.7919	−3.4134

solar cycles 22 and 23 than in the cycles 21 and 24. During the cycle 23, the two parameters derived through Choices U and B decreased in values toward the sunspot maximum and suddenly increased soon after the maximum and decreased again in the descending phase. We can see a weak but similar trend in Choice E, while such trend is not found in the cycle 22. These trends are consistent with the fact that the solar wind plasma in recent years is substantially different from that in the solar cycles 22 and 23. We need further investigations to make reasonable descriptions on the long-term variations of relationships among the solar wind plasma variables because the parameters shown in Figure 8 disperse substantially around the polynomial curves and the differences between Choice E and Choice U or B are large. The analysis shown in Figure 8, however, can be a first step toward better characterizing temporal evolutions of the solar wind plasma over cycles of solar magnetic activity.

Lastly, we attempt to relate the differences between the optimized solutions and the reference Choice H with the coronal dynamics. For each CR period, the radial component of magnetic field (B_r) on the inner boundary sphere at 50 R_s is calculated from the values on the source surface of the PFSS model and fixed all through the calculations of MHD-IPS tomography and the iterative optimization of parameterized functions. Therefore, the boundary radial component of magnetic field is a parameter with which we can straightforwardly relate the derived solar wind plasma quantities with the global coronal magnetic field that is believed to play primary roles in coronal heating and acceleration. In this context, we calculate the differences of plasma density, temperature, and energy density between Choice H and the optimized functions and compare with the boundary magnetic field. Figure 9 compares the differences with the absolute value of radial component of the boundary magnetic field ($|B_r|$). The energy density is here the sum of kinetic and thermal energy, $\rho V_r^2/2 + P_g/(\gamma - 1)$. The gray scales represent numbers of occurrence sampled in equi-area (equisine latitude and equilongitude) spacing for all CR periods. A white line in each box shows the least squares fitting line, and its slope and intercept are denoted near the right bottom corner together with the correlation coefficient. Table 3 tabulates the three statistic values.

All of the differences of plasma quantities shown in Figure 9 have positive correlations to $|\vec{B}|$ on the inner boundary sphere hence on the source surface of PFSS model. The positive correlations from this statistical analysis is similar to the tendency of solar wind speed and the source-surface magnetic field found in the

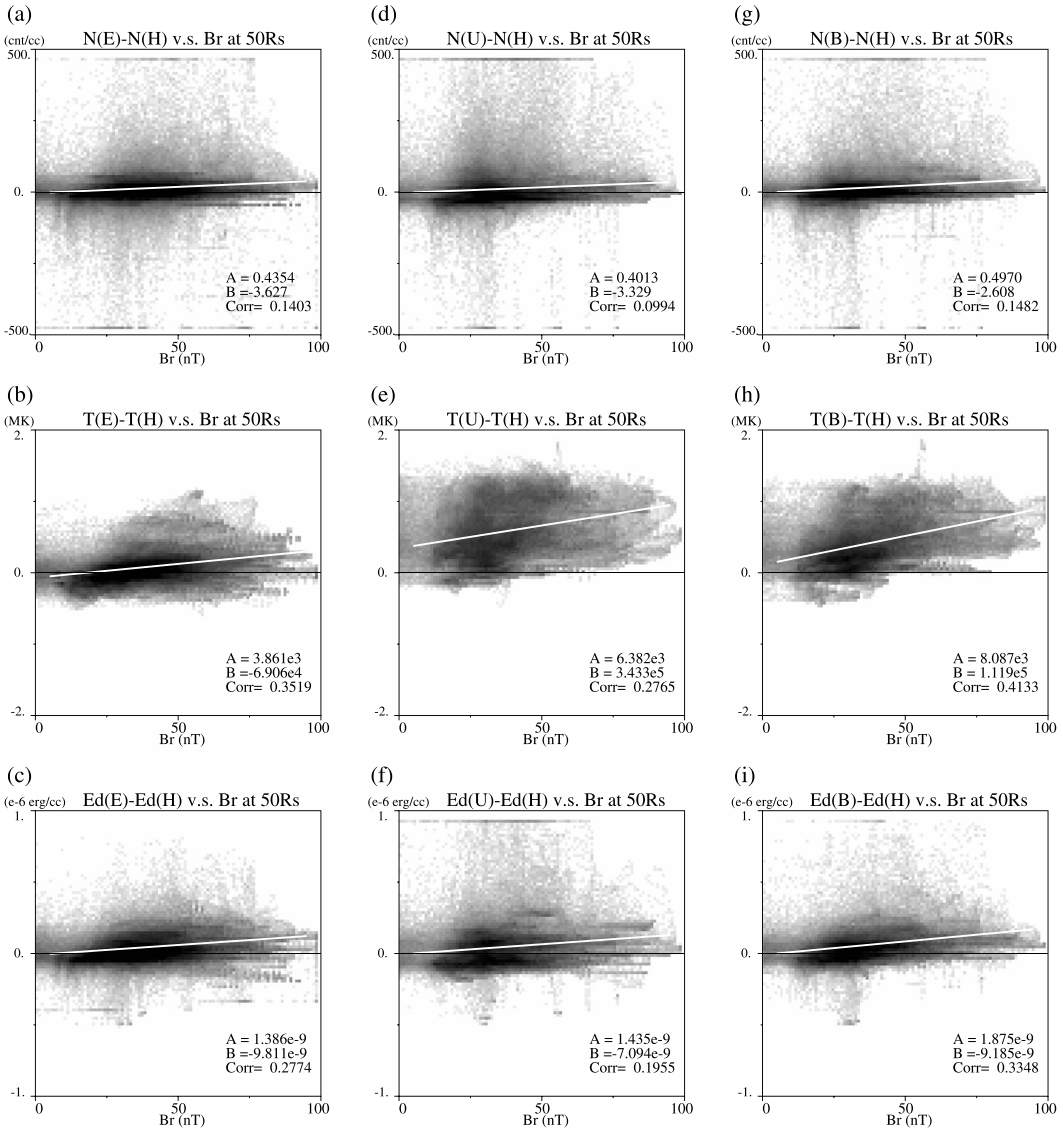

Figure 9. The difference (increase) of plasma quantities from Choice H (ΔT) as function of magnetic field strength $|B_r|$ at 50 R_s. From top to bottom, the plasma number density, temperature, and sum of kinetic and thermal energy density are shown. From left to right, the scatterplots for Choices E, U, and B are shown. Gray scales represent logarithm of area-weighted occurrence over periods for which the optimization successfully yielded a set of converged functions. A linear fitting line is placed in each box for reference, and the values of slope (A) and intercept (B) of the line and the correlation coefficient (Corr.) are placed near the right bottom corner in each box. Notice the positive correlation in all nine plots.

IPS analysis by *Kojima et al.* [2004] and derived from the theoretical study by *Sukuzi and Inutsuka* [2005] and *Suzuki* [2006]. The numbers tabulated in Table 3 determine values to be added to the reference Helios-based $N(V)$ and $T(V)$. The expression of density and temperature, in the form of $N(V, |B_r|)$ and $T(V, |B_r|)$, is physically and practically favored because two MHD variables, plasma density and temperature, at a certain position on 50 R_s sphere can be calculated from other MHD variables at the same position.

The zero value of $|B_r|$ corresponds to the top of a closed-field structure of PFSS solution (or a coronal streamer of actual solar corona) where the actual magnetic field strength ($|\vec{B}|$) is not necessarily zero. Hence, the intercept values listed in Table 3 do not immediately pertain to the additional thermal (nonmagnetic) contribution in corona heating and acceleration process; it simply provides the difference in minimum amount of total energy the solar wind plasma can receive in a certain time of interest from that in the Helios mission period. The values of slope and intercept tabulated in Table 3 imply that the coronal field strength, and probably

Table 3. Slope, Intercept, and Correlation Coefficient of Linear Fitting Lines in Figure 9

Figure 9 Label	Variable (v.s $\lvert B_r \rvert$)	Slope	Intercept	Correlation Coefficient
a	N(E)-N(H)	+0.4354 (count/cm^3/nT)	−3.627 (count/cm^3)	+0.1403
b	T(E)-T(H)	+3.861E3 (°/nT)	−6.906E4 (degree)	+0.3519
c	Ed(E)-Ed(H)	+1.386E−9 (erg/cm^3/nT)	−9.811E−9 (erg/cm^3)	+0.2774
d	N(U)-N(H)	+0.4013 (count/cm^3/nT)	−3.329 (count/cm^3)	+0.0994
e	T(U)-T(H)	+6.382E3 (°/nT)	+3.433E5 (deg)	+0.2765
f	Ed(U)-Ed(H)	+1.435E−9 (erg/cm^3/nT)	−7.094E−9 (erg/cm^3)	+0.1955
g	N(B)-N(H)	+0.4970 (count/cm^3/nT)	−2.608 (count/cm^3)	+0.1482
h	T(B)-T(H)	+8.087E3 (°/nT)	+1.119E5 (deg)	+0.4133
i	Ed(B)-Ed(H)	+1.875E−9 (erg/cm^3/nT)	−9.185E−9 (erg/cm^3)	+0.3348

the shapes of each magnetic flux tube (e.g., latitudinal and longitudinal displacements from photosphere to source surface or total length of each flux tube and solar coronal activities in its vicinity) can be decisive factors of the solar wind speed and other plasma quantities. The reliable models relating the flux expansion factor and solar wind speeds, such as the WSA model [*Wang and Sheeley*, 1990; *Arge and Pizzo*, 2000; *Arge et al.*, 2003; *Wang*, 2010], do not directly include the magnetic field strength or yield plasma density or temperature; therefore, the relationship of plasma energy, density, and temperatures with magnetic field tabulated in Table 3 can help enhance accuracy of this model to better predict solar wind speed in recent periods of weak solar magnetic field. The contribution of magnetic field to the coronal heating in the context of its global coronal structure would be investigated using the obtained relationship shown in Figure 9: It is a reasonable expectation that the analysis expressing the solar wind energy and other plasma quantities in terms of photospheric and source-surface magnetic field strength, coronal magnetic shapes, position and solar activity in vicinity, and probably time (solar cycle number and phase) will give reasonable quantitative descriptions on the coronal heating and acceleration processes.

The optimization procedures for relationship functions, $N(V)$ and $T(V)$, and the MHD-IPS tomography employ several assumptions, in part for minimizing complexity in computations. For example, in the MHD-IPS tomography, a LOS IPS data value that is significantly different from three-dimensional MHD solution is regarded as an interplanetary passage of CME or flare-related event and discarded out. This filtering is essential in the tomographic method that primarily seeks steady solutions. However, the MSE minimization process presented in this study does not distinguish the disturbance from the quiet ambient wind in the in situ data. For further improvement in optimizing the relation functions, we need to include an algorithm to filter out the data of disturbed solar wind in the optimization process.

In this work, we do not analyze the results in terms of solar cycle number or phase, or latitudinal distribution. In the future, the methods presented in this study would be applied to quantitatively address the weak solar wind measured by Ulysses in late solar cycle 22 [e.g., *McComas et al.*, 2008, 2013; *Sokol et al.*, 2015] and the latitudinal structures of solar wind [e.g., *Sokol et al.*, 2013]. These points are important for understanding the coronal dynamics as the source of solar wind that exhibit various, long-term variations over solar cycles.

Acknowledgments
The IPS observations have been carried out under the solar wind program of the Institute for Space-Earth Environment Research (ISEE) of Nagoya University. This work was supported by JSPS KAKENHI, grant (A) 25247079. The IPS data are available at http://stsw1.isee.nagoya-u.ac.jp/index-e.html. The authors use the synoptic maps of solar photospheric magnetic field at the Wilcox Solar Observatory (WSO), Stanford University (http://wso.stanford.edu). The OMNI and COHO data sets compiled and maintained at the Space Physics Data Facility (SPDF) of NASA/GFSC are used for the comparison with our simulation data. Both OMNI and COHO data sets are obtained through http://omniweb.gsfc.nasa.gov/. The sunspot number data we used in this paper are from the Sunspot Index and Long-term Solar Observations (SILSO) data set at Royal Observatory of Belgium, Brussels (http://sidc.oma.be/silso/DATA/monthssn.dat). The computations presented in this study were conducted on the CX400 and FX100 computer systems at Information Technology Center of Nagoya University, Japan, under the computational joint research program of the Institute for Space-Earth Environment Research, Nagoya University.

References

Altschuler, M. D., and G. Newkirk Jr. (1969), Magnetic fields and the structure of the solar corona. I: Methods of calculating coronal fields, *Sol. Phys.*, *9*, 131–149, doi:10.1007/BF00145734.

Arge, C. N., and V. J. Pizzo (2000), Improvement in the prediction of solar wind conditions using near-real time solar magnetic field update, *J. Geophys. Res.*, *105*(A5), 10,465–10,480, doi:10.1029/1999JA900262.

Arge, C. N., D. Odstrcil, V. J. Pizzo, and L. R. Mayer (2003), Improved method for specifying solar wind speed near the Sun, *AIP Conf. Proc.*, *679*, 190, doi:10.1063/1.1618574.

Detman, T. R., D. S. Intriligator, M. Dryer, W. Sun, C. S. Deehr, and J. Intriligator (2011), The influence of pickup protons, from interstellar neutral hydrogen, on the propagation of interplanetary shocks from the Halloween 2003 solar events to ACE and Ulysses: A 3-D MHD modeling study, *J. Geophys. Res.*, *116*, A93195, doi:10.1029/2010JA015803.

Dryer, M. (1994), Interplanetary studies: Propagation of disturbances between the Sun and the magnetosphere, *Space Sci. Rev.*, *67*, 363–419, doi:10.1007/BF00756075.

Feng, X. S., L. P. Yang, C. Q. Xiang, S. T. Wu, Y. F. Zhou, and D. K. Zhong (2010), Three-dimensional solar wind modeling from the Sun to Earth by a SIP-CESE MHD model with a six-component grid, *Astrophys. J.*, *723*, 300–319, doi:10.1088/0004-637X/723/1/300.

Feng, X., et al. (2012), Validation of the 3D AMR SIP-CESE solar wind model for four Carrington rotations, *Sol. Phys.*, *279*, 207, doi:10.1007/s11207-012-9969-9.

Feng, X. S., X. Ma, and C. Xiang (2015), Data-driven modeling of the solar wind from 1 R_s to 1 AU, *J. Geophys. Res. Space Physics*, *120*, 10,159–10,174, doi:10.1002/2015JA021911.
Hayashi, K., M. Kojima, M. Tokumaru, and K. Fujiki (2003), MHD tomography method using interplanetary scintillation measurement, *J. Geophys. Res.*, *108*(A3), 1102, doi:10.1029/2002JA009567.
Hayashi, K. (2005), Magnetohydrodynamic simulations of the solar corona and solar wind using a boundary treatment to limit solar wind mass flux, *Astrophys. J.*, *161*, 480, doi:10.1086/491791.
Hayashi, K., X. P. Zhao, and Y. Liu (2006), MHD simulation of two successive interplanetary disturbances driven by Cone-model parameters in IPS-based solar wind, *Geophys. Res. Lett.*, *33*, L20103, doi:10.1029/2006GL027408.
Hayashi, K., H. Washimi, and M. Tokumaru (2011), The MHD simulation of the inner heliosphere over 9 years using the observation-based time-varying boundary data, in *Proceedings of the 10th Annual International Astrophysics Conference (AIAC)*, vol. 1436, pp. 308–313, Am. Inst. Phys. Conf. Proc., Maui, Hawaii.
Hayashi, K. (2012), An MHD simulation model of time-dependent co-rotating solar wind, *J. Geophys. Res.*, *117*, A08105, doi:10.1029/2011JA017490.
Hoeksema, J. T., J. M. Wilcox, and P. H. Scherrer (1983), The structure of the heliospheric current sheet—1978–1982, *J. Geophys. Res.*, *88*, 9910, doi:10.1029/JA088iA12p09910.
Hoeksema, J. T. (1995), The large-scale structure of the heliospheric current sheet during the ULYSSES Epoch, *Space Sci. Rev.*, *72*, 137–148, doi:10.1007/BF00768770.
Intriligator, D. S., J. Intriligator, W. D. Miller, W. R. Webber, R. B. Decker, W. Sun, T. Detman, M. Dryer, and C. Deehr (2010), Voyager 2 high energy ions near the outward moving termination shock, *AIP Conf. Proc.*, *1302*, 148, doi:10.1063/1.3529963.
Jackson, B. V., P. L. Hick, M. Kojima, and A. Yokobe (1998), Heliospheric tomography using interplanetary scintillation observations: 1. Combined Nagoya and Cambridge data, *J. Geophys. Res.*, *103*, 12,049–12,067, doi:10.1029/97JA02528.
Jackson, B. V., P. P. Hick, A. Buffington, M. M. Basi, J. M. Clover, M. Tokumaru, M. Kojima, and K. Fujiki (2011), Three-dimensional reconstruction of heliospheric structure using iterative tomography: A review, *J. Atmos. Sol. Terr. Phys.*, *73*, 1214–1227, doi:10.1016/j.jastp.2010.10.007.
Kataoka, R., T. Ebisuzaki, K. Kusano, D. Shiota, S. Inoue, T. T. Yamamoto, and M. Tokumaru (2009), Three-dimensional MHD modeling of the solar wind structures associated with 13 December 2006 coronal mass ejection, *J. Geophys. Res.*, *114*, A10102, doi:10.1029/2009JA014167.
Kim, T. K., N. V. Pogorelov, S. N. Borovikov, B. V. Jackson, H.-S. Yu, and M. Tokumaru (2014), MHD heliosphere with boundary conditions from a tomographic reconstruction using interplanetary scintillation data, *J. Geophys. Res. Space Physics*, *119*, 7981–7997, doi:10.1002/2013JA019755.
Kojima, M., M. Tokumaru, H. Watanabe, and A. Yokobe (1998), Heliospheric tomography using interplanetary scintillation observations: 2. Latitudinal and heliocentric distance dependence of solar wind structure at 0.1-1 AU, *J. Geophys. Res.*, *103*, 1981–1989, doi:10.1029/97JA02162.
Kojima, M., K. Fujiki, M. Hirano, M. Tokumaru, T. Ohmi, and K. Hakamada (2004), Solar wind properties from IPS observations, in *The Sun the Heliosphere as an Integrated System*, edited by G. Poletto and S. T. Suess, pp. 147–178, Kluwer, Dordrecht, doi:10.1007/978-1-4020-2666-9_6.
McComas, D. J., R. W. Ebert, H. A. Elliott, B. E. Goldstein, J. T. Gosling, N. A. Schwadron, and R. M. Skoug (2008), Weaker solar wind from the polar coronal holes and the whole Sun, *Geophys. Res. Lett.*, *35*(18), L18103, doi:10.1029/2008GL034896.
McComas D. J., N. Angold, H. A. Elliott, G. Livadiotis, N. A. Schwadron, R. M. Skoug, and C. W. Smith (2013), Weakest solar wind of the space age and the current mini solar maximum, *Astrophys. J.*, *779*(2), 2, doi:10.1088/0004-637X/779/1/2.
Odstrcil, D., and V. J. Pizzo (2009), Numerical heliospheric simulations as assisting tool for interpretation of observations by STEREO heliospheric imagers, *Sol. Phys.*, *259*, 297–309, doi:10.1007/s11207-009-9449-z.
Owens, M. J., C. N. Arge, H. E. Spence, and A. Pembroke (2005), An event-based approach to validating solar wind speed predictions: High-speed enhancements in the Wang-Sheeley-Arge model, *J. Geophys. Res.*, *110*, A12105, doi:10.1029/2005JA011343.
Pogorelov, N. V., S. T. Suess, S. N. Borovikov, R. W. Ebert, D. J. McComas, and G. P. Zank (2013), Three-dimensional features of the outer heliosphere due to coupling between the interstellar and interplanetary magnetic fields: IV. Solar cycle model based on Ulysses observations, *Astrophys. J.*, *772*, 2, doi:10.1088/0004-637X/772/1/2.
Riley, P., Z. Mikic, R. Lionello, J. A. Linker, N. A. Schwadron, and D. J. McComas (2010), On the relationship between coronal heating, magnetic flux, and the density of the solar wind, *J. Geophys. Res.*, *115*, A06104, doi:10.1029/2009JA015131.
Riley, P., R. Lionello, J. A. Linker, Z. Mikic, J. Luhmann, and J. Wijaya (2011), Global MHD modeling of the solar corona and inner heliosphere for the whole heliosphere interval, *Sol. Phys.*, *274*, 361–377, doi:10.1007/s11207-010-9698-x.
Schatten, K. H., J. M. Wilcox, and N. F. Ness (1969), A model of interplanetary and coronal magnetic field, *Sol. Phys.*, *6*, 442–455, doi:10.1007/BF00146478.
Sokol, J. M., M. Bzowski, M. Tokumaru, K. Fujiki, and D. J. McComas (2013), Heliolatitude and time variations of solar wind structure from in-situ measurements and interplanetary scintillation observations, *Sol. Phys.*, *285*, 167–200.
Sokol, J. M., P. Swaszyna, M. Bzowski, and M. Tokumaru (2015), Reconstruction of helio-latitudinal structure of the solar wind proton speed and density, *Sol. Phys.*, *290*, 2589–2615, doi:10.1007/s11207-015-0800-2.
Suzuki, T. K., and S. Inutsuka (2005), Making the corona and the fast solar wind: A self-consistent simulation for the low-frequency Alfven waves from the photosphere to 0.3 AU, *Astrophys. J.*, *632*(1), L49, doi:10.1086/497536.
Suzuki, T. K. (2006), Forecasting solar wind speed, *Astrophys. J.*, *640*, L75, doi:10.1086/503102.
Tokumaru, M., M. Kojima, K. Fujiki, and K. Hayashi (2009), Non-dipolar solar wind structure observed in the cycle 23/24 minimum, *Geophys. Res. Lett.*, *36*, L09101, doi:10.1029/2009GL037461.
Tokumaru, M., M. Kojima, and K. Fujiki (2010), Solar cycle evolution of the solar wind speed distribution from 1985 to 2008, *J. Geophys. Res.*, *115*, A04102, doi:10.1029/2009JA014628.
Tokumaru, M., M. Kojima, and K. Fujiki (2012), Long-term evolution in the global distribution of solar wind speed and density fluctuations during 1997–2009, *J. Geophys. Res.*, *117*(A6), A06108, doi:10.1029/2011JA017379.
Tokumaru, M., K. Fujiki, and T. Iju (2015), North-south asymmetry in global distribution of the solar wind speed during 1985–2013, *J. Geophys. Res. Space Physics*, *120*, 3283, doi:10.1002/2014JA020765.
Totten, T. L., J. W. Freeman, and S. Arya (1995), An empirical determination of the polytropic index for the free-streaming solar wind using Helios 1 data, *J. Geophys. Res.*, *100*, 13–17, doi:10.1029/94JA02420.
Usmanov, A. V., M. L. Goldstein, B. P. Besser, and J. M. Fritzer (2000), A global MHD solar wind model with WKB Alfven waves: Comparison with Ulysses data, *J. Geophys. Res.*, *105*(A6), 12,675–12,695, doi:10.1029/1999JA000233.
Usmanov, A. V., W. H. Matthaeus, B. A. Breech, and M. L. Goldstein (2011), Solar wind modeling with turbulence transport and heating, *Astrophys. J.*, *727*, 84–96, doi:10.1088/0004-637X/727/2/84.

Wang, Y.-M., and N. R. Sheeley Jr., (1990), Solar wind speed and coronal flux-tube expansion, *Astrophys. J.*, *335*, 762, doi:10.1086/168805.
Wang, Y.-M. (2010), On the relative constancy of the solar wind mass flux at 1 AU, *Astrophys. J.*, *715*, L121–L127, doi:10.1088/2041-8205/715/2/L121.
Washimi, H., G. P. Zank, Q. Hu, T. Tanaka, K. Munakata, and H. Shinagawa (2011), Realistic and time-varying outer heliospheric modeling, *Mon. Not. R. Astron. Soc.*, *416*, 1475–1485, doi:10.1111/j.1365-2966.2011.19144.x.
Wu, C.-C., S. T. Wu, M. Dryer, C. D. Fry, D. Berdichevsky, Z. Smith, T. Detman, N. Gopalswamy, R. Skoug, T. Zurbuchen, and C. Smith (2005), Flare-generated shock evolution and geomagnetic storms during the Halloween 2003 epoch: 29 October to 2 November, *J. Geophys. Res.*, *110*, A09S17, doi:10.1029/2005JA011011.
Wu, C.-C., M. Dryer, S. T. Wu, B. E. Wood, C. D. Fry, K. Liou, and S. Plunkett (2011), Global three-dimensional simulation of the interplanetary evolution of the observed geoeffective coronal mass ejection during the epoch 1–4 August 2010, *J. Geophys. Res.*, *116*, A12103, doi:10.1029/2011JA016947.
Wu, S. T., Y. Zhou, C. Jiang, X. S. Feng, C. C. Wu, and Q. Hu (2016), A data-constrained three-dimensional magnetohydrodynamic simulation model for a coronal mass ejection initiation, *J. Geophys. Res. Space Physics*, *121*, 1009–1023, doi:10.1002/2015JA021615.
Yang, L. P., X. S. Feng, C. Q. Xiang, Y. Liu, X. P. Zhao, and S. T. Wu (2012), Time-dependent MHD modeling of the global solar corona for year 2007: Driven by daily-updated magnetic field synoptic data, *J. Geophys. Res.*, *117*, A08110, doi:10.1029/2011JA017494.
Yang, L. P., X. S. Feng, J. S. He, L. Zhang, and M. Zhang (2016), A self-consistent numerical study of the global solar wind driven by the unified nonlinear Alfven wave, *Sol. Phys.*, *291*, 953–963, doi:10.1007/s11207-016-0861-x.